



**Contrasting role of small metallic elements (M=Cu, Zn, Ni)
in enhancing thermoelectric performance of n-type
PbM_{0.01}Se**

Journal:	<i>Journal of Materials Chemistry A</i>
Manuscript ID	TA-ART-01-2020-000174.R1
Article Type:	Paper
Date Submitted by the Author:	27-Feb-2020
Complete List of Authors:	<p>Qian, Xin; Beihang University, School of Materials Science and Engineering</p> <p>Wang, Dongyang; Beihang University, wangdongyang@buaa.edu.cn</p> <p>Zhang, Yang; National University of Singapore, Department of Materials Science and Engineering</p> <p>Wu, Haijun; National University of Singapore, Department of Materials Science and Engineering</p> <p>Pennycook, Stephen; National University of Singapore, Materials Science and Engineering</p> <p>Zheng, Lei; Beihang University, School of Materials Science and Engineering Beijing</p> <p>Poudeu, Pierre Ferdinand; University of Michigan, Department of Materials Science and Engineering; University of Michigan, Department of Materials Science and Engineering</p> <p>Zhao, Li-Dong; Beihang University, Materials Science and Engineering</p>

Contrasting role of small metallic elements (M=Cu, Zn, Ni) in enhancing the thermoelectric performance of n-type $\text{PbM}_{0.01}\text{Se}$

Xin Qian,^a Dongyang Wang,^a Yang Zhang,^b Haijun Wu,^{b,*} Stephen J. Pennycook,^b Lei Zheng,^{a,*} Pierre F. P. Poudeu,^{c,*} Li-Dong Zhao^{a,**}

^a *School of Materials Science and Engineering, Beihang University, Beijing 100191, China.*

^b *Department of Materials Science and Engineering, National University of Singapore, Singapore 117575, Singapore*

^c *Laboratory for Emerging Energy and Electronic Materials, Department of Materials Science and Engineering, University of Michigan, Ann Arbor, MI, 48109, USA.*

Corresponding authors: wu.haijun@u.nus.edu, zhenglei@buaa.edu.cn, ppoudeup@umich.edu, zhaolidong@buaa.edu.cn

Abstract

The metallic elements with a small atomic radius can not only compensate for the intrinsic vacancies to improve the carrier mobility, but also can form interstitials to reduce lattice thermal conductivity. In this work, we investigate the contrasting role of three different metallic elements with small atomic radius on the thermoelectric properties of *n*-type $\text{PbM}_{0.01}\text{Se}$ ($M=\text{Cu, Zn, Ni}$). We find that all the metallic elements can increase the carrier concentration as electron donors and improve the electrical transport properties. In addition, the lattice thermal conductivity of PbSe can be significantly decreased through the formation of interstitials by the incorporated extra metallic elements. We also find that the $\text{PbCu}_{0.01}\text{Se}$ sample exhibits a unique and complex behavior compared with the other samples due to the diffusion and the thermally activated oxidation of Cu^+ ions. When the temperature increased to 673 K, the carrier concentration of $\text{PbCu}_{0.01}\text{Se}$ sample increases suddenly and continues to increase by nearly two folds, which we ascribe to the release of 3d orbital electrons in Cu^+ ions. This results in a strong decoupling of the charge and heat transport in the material, which can be manifested by the overestimation of the electronic thermal conductivity when assuming strong electron-phonon coupling in Wiedemann-Franz law. A maximum ZT of ~ 1.6 can be reached at 773 K and the average ZT of ~ 0.96 can be achieved in $\text{PbCu}_{0.01}\text{Se}$. Our results demonstrate the exceptional contrasting behavior of Cu in PbSe by comparing with Zn and Ni, and the thermoelectric performance of *n*-type PbSe can be enhanced through the introduction of extra metallic elements with small radius.

Keywords: Thermoelectric; *n*-type PbSe ; small metallic elements; lattice thermal conductivity; ZT value

1. Introduction

Thermoelectric materials, which enable the direct conversion between heat and electricity through the movement of internal carriers, have received extensive attention.¹⁻³ However, low energy conversion efficiency has prevented the thermoelectric technology from achieving large-scale applications.⁴⁻⁶ The efficiency of thermoelectric materials can be evaluated by the dimensionless figure of merit, $ZT = S^2\sigma T/\kappa$, where S , σ , κ , and T are the Seebeck coefficient, electrical conductivity, thermal conductivity, and absolute temperature, respectively.⁷⁻⁹ Thus it can be seen that high-performance thermoelectric materials need to have high electrical conductivity, large Seebeck coefficient and low thermal conductivity.¹⁰⁻¹² In the past decades, researchers have proposed a number of strategies to improve the thermoelectric performance. For instance, improving the Seebeck coefficient through manipulation of the band structures^{13, 14} and introduction of resonant impurity levels^{15, 16}, and reducing lattice thermal conductivity by designing hierarchical architectures *via* enhancement of all-scale phonon scattering.^{17, 18}

It is well known that the lattice thermal conductivity is contributed by the propagation of phonons carrying heat.¹⁹ Enhancing the phonons scattering by introducing crystal defects is the most effective strategy for decreasing lattice thermal conductivity. The conventional elements alloying method can introduce a large number of point defects, dislocations and nanostructures, which is one of the most commonly used means to suppress the lattice thermal conductivity and improve the thermoelectric performance.²⁰ Normally, the alloying methods require solid solution of isovalent elements and a large fraction. However, the isovalent alloying is usually accompanied by damaging electrical conductivity, thus the power factor, such as in PbSe-SrSe,²⁰ PbSe-PbS,²¹ and PbTe-PbS,²² which is unfavorable for the ultimate improvement of the thermoelectric performance.

In recent years, doping/alloying metallic elements with small atomic radius, such as Cu and Ag, in IV-VI compounds has received more attention because these elements can enter the crystal lattice easily to form interstitials. These interstitials can reduce the

lattice thermal conductivity significantly while maintain a high carrier mobility. For example, in *n*-type PbTe-Cu₂Te²³, the Cu interstitials coupled with Cu-rich precipitates lead to a very low lattice thermal conductivity of $\sim 0.38 \text{ W m}^{-1}\text{K}^{-1}$, which approaches the theoretical limitation for PbTe. In addition, a small amount of Cu atoms can compensate for the intrinsic Pb vacancies, which can enormously improve the carrier mobility.²³ Apart from that, in polycrystalline SnSe doping with 1 % Cu, the lattice thermal conductivity can be reduced to as low as $\sim 0.20 \text{ W m}^{-1}\text{K}^{-1}$ at 873 K because the Cu atomic point defect significantly contributes to phonons scattering.²⁴ Moreover, by introducing excess of metallic Ag in PbTe-Ag₂Te composite, the thermoelectric efficiency can be improved by $\sim 50 \%$, which is attributed to increase solubility of Ag into the PbTe lattice with rising temperature.²⁵

The above results motivated us to explore whether other elements with small atomic radius can produce the same performance. Recently, we found that the thermoelectric performance of *n*-type PbSe can be significantly improved through the introduction of a small amount of Zn atoms.²⁶ However, we have not found that the carrier concentration of Zn doped PbSe will increase at high temperature like doping with Cu.²⁷ In this work, we further investigated the effects of three different metallic elements with small atomic radius, Cu (1.28 Å), Zn (1.37 Å) and Ni (1.25 Å), on the thermoelectric properties of *n*-type PbSe. The present research results indicated that the effects of Zn and Ni on the thermoelectric properties of *n*-type PbSe are similar while the case of Cu is extremely complicated. These three elements all act as electron donors to increase the carrier concentration in *n*-type PbSe because their 4s electrons can be removed easily through minimal thermal activation. However, we found that when the temperature increased to 673 K, the 3d electron of the Cu⁺ ions receives enough energy to escape the attractive force from the nucleus. Therefore, the temperature dependent carrier concentration curve for the PbCu_{0.01}Se sample increases suddenly at 673 K and continues to increase by nearly two folds. In addition, we observed that the large increase in the electrical conductivity above 673 K, which results from the sudden increase in the carrier concentration, does not translate to a large increase in the total thermal conductivity for the PbCu_{0.01}Se sample. This implies a strong decoupling of the

charge and heat transport in the sample. Under such condition, the use of the Wiedemann-Franz law that assumes strong electron-phonon coupling leads to an overestimation of the electronic thermal conductivity, which is manifested by an unreasonably low lattice thermal conductivity.

Although the lattice thermal conductivity, due to the diffusion of Cu^+ ions, becomes hard to evaluate, the measured total thermal conductivity is not altered by the observed departure from the Wiedemann-Franz law. Therefore, a maximum ZT value of ~ 1.6 at 773 K and an average ZT of ~ 0.96 can be achieved in the $\text{PbCu}_{0.01}\text{Se}$ sample. This study demonstrates the exceptional effect of Cu atom, by comparison to Zn and Ni, on the thermoelectric properties of n -type PbSe.

2. Experimental section

Starting materials. High-purity raw materials, Pb chunk (99.999%, Aladdin, China), Se chunk (99.999%, Aladdin, China), Cu shot (99.99%, Aladdin, China), Zn shot (99.99%), Ni powder (99.99%, Aladdin, China) and PbBr_2 powder (99.99%, Aladdin, China) were used for the sample preparation.

Sample preparation. The $\text{PbM}_{0.01}\text{Se}$ ($M=\text{Cu}, \text{Zn}, \text{Ni}$) ingots doped with 0.1 % PbBr_2 were prepared through melting methods. It should be noted that all the samples are doped with 0.1 % PbBr_2 to optimize the carrier concentration, so the samples were not named with Br for the sake of simplicity. The raw materials weighed according to the above stoichiometric ratio were first placed in small quartz tubes (~ 10 mm in diameter) under an N_2 -filled glovebox. Then, the tubes were flame-sealed under vacuum ($\sim 10^{-4}$ Torr) and every tube was inserted in a large quartz tube (~ 20 mm in diameter) to avoid oxidation of the sample if the tubes break during the synthesis process. The sealed large quartz tubes were slowly heated from room temperature to 1423 K for 24 h, soaked at 1423 K for 12 h and subsequently cooled to room temperature in the furnace. The obtained ingots were ground into fine powders using a mortar and pestle and densified under vacuum at 873 K for 5 minutes using a spark plasma sintering (SPS) system (SPS-211LX, Fuji Electronic Industrial Co., Ltd) with

an axial pressure of 50 MPa. Highly densified ($> 96\%$ of theoretical density) disk-shaped pellets with dimensions of $\Phi 15 \text{ mm} \times 9 \text{ mm}$ were obtained.

Thermoelectric properties measurement. The SPS-processed pellets were cut into bars with dimensions of $3 \times 3 \times 12 \text{ mm}^3$ for the Seebeck coefficient and electrical resistivity measurement, which was conducted from room temperature to 873 K with CTA instrument (Cryoall, China) under the protection of helium gas. The surfaces of the bars were coated with a thin layer of boron nitride (BN) to protect the instrument from sample evaporation. Square shape samples with dimensions of $8 \times 8 \times 0.6 \text{ mm}^3$ were cut for Hall effect measurement using Lake Shore 8400 Series, Model 8404, USA. The Hall carrier concentration (n_{H}) of the samples were measured in the temperature range from 300 K to 873 K under a reversible magnetic field (0.9 T) *via* the Van der Pauw method. The carrier mobility (μ_{H}) was calculated using the relationship $\mu_{\text{H}} = \sigma / (e \cdot n_{\text{H}})$ with σ being the electrical conductivity obtained from the CTA instrument. The typical thin square pieces with dimensions of $8 \times 8 \text{ mm}$ and 1~2 mm in thickness were used for the measurement of thermal diffusivity (D), which were conducted with a Netzsch LFA 457 laser flash instrument. The pieces were coated with a thin layer of graphite to minimize errors from the material emissivity. The thermal diffusivity data were analyzed using a Cowan model with pulse correction. The overall uncertainty for all measurements involved in the ZT calculation was less than $\sim 20 \%$.

X-ray diffraction and electron microscopy. The phase composition and structure of the samples were determined through powder X-ray diffraction (XRD), which were conducted using a D/max 2500PC X-ray diffractometer with Cu $K\alpha$ ($\lambda = 1.5418 \text{ \AA}$) radiation in a reflection geometry on an Inel diffractometer operating at 40 kV and 20 mA and equipped with a position-sensitive detector. The scanning speed was 6° per minute and the scanning angles ranged from 20° to 80° . The microstructures of the bulk samples were characterized using transmission electron microscopy (TEM), which were carried out with a JEOL ARM200F atomic resolution analytical electron microscope operated at 200 kV.

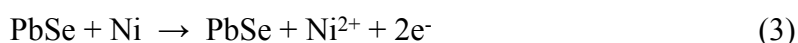
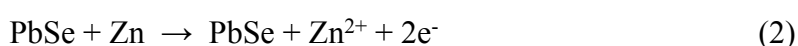
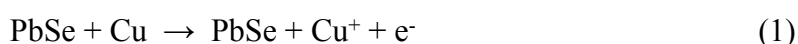
3. Results and discussion

Our previous work showed that intrinsic Pb vacancies are present in pristine PbSe, which lead to its weak *p*-type conductive behavior.²⁶ Therefore, we first optimize the carrier concentration by doping with 0.2 % Br in the Se site in order to create *n*-type semiconductor. Then, all the metallic elements (Cu, Zn, Ni) are introduced as extra element instead of substituting for Pb. Therefore, in addition to compensating the intrinsic Pb vacancies, the added metallic atoms also can form interstitials within the PbSe crystal lattice, which can reduce lattice thermal conductivity. The powder XRD patterns of $\text{PbM}_{0.01}\text{Se}$ ($\text{M}=\text{Cu, Zn, Ni}$) samples prepared by the melting method are depicted in Fig. 1. It can be seen that all the peaks are indexed with the standard face-centered cubic (fcc) structure (space group Fm-3m) of PbSe and no impurity phase could be detected.²⁸

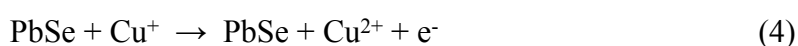
Our previous work revealed that the added metallic elements first compensate for intrinsic Pb vacancies of PbSe and then form interstitials.^{23, 26} Regardless of their location within the crystal lattice (Pb vacancies or form interstitials), the carrier concentration of the resulting *n*-type $\text{PbM}_{0.01}\text{Se}$ sample should increase as shown in Fig. 2(a). It is worth noting that the carrier concentration of $\text{PbZn}_{0.01}\text{Se}$ and $\text{PbNi}_{0.01}\text{Se}$ samples are similar and remain nearly temperature independent, while the carrier concentration of the $\text{PbCu}_{0.01}\text{Se}$ sample is about half than that of the former two samples at the temperatures below 673 K. However, when the temperature increases to 673 K, the carrier concentration of the $\text{PbCu}_{0.01}\text{Se}$ sample suddenly increases within a narrow temperature window approaching that of $\text{PbZn}_{0.01}\text{Se}$ and $\text{PbNi}_{0.01}\text{Se}$ samples at 873 K. Similar increase of the carrier concentration with the increasing temperature was also observed in PbTe-Cu ²³ and PbS-Cu ²⁹, which further confirms the unique behavior of Cu atoms as dopants in PbX ($\text{X} = \text{S, Se, Te}$) matrix. The carrier mobility of the PbSe sample is also improved due to the compensation of Pb vacancy as depicted in Fig. 2(b). The carrier scattering mechanism in the sample can be obtained by analyzing the temperature dependence of the carrier mobility.^{26, 30} Vacancy scattering is the dominating mechanism for pristine PbSe at low temperature and gradually turns into

acoustic phonon scattering with increasing temperature. By introducing metallic elements, the intrinsic Pb vacancies in PbSe are compensated. Therefore, acoustic phonon scattering dominates in the whole temperature range. It should be noted that the carrier mobility of the $\text{PbCu}_{0.01}\text{Se}$ samples shows an abnormal behavior at high temperatures, which suggests that acoustic phonon scattering is not the predominant scattering mechanism. The observed simultaneous increase in the carrier mobility and the carrier concentration at 673 K implies a weak coupling between charge and heat transport within the $\text{PbCu}_{0.01}\text{Se}$ sample, which could lead to a poor estimation of the Lorenz number as will be discussed later.

The unique behavior of the $\text{PbCu}_{0.01}\text{Se}$ sample stems from the fact that incorporated elemental Cu can adopt two stable valence states depending on the temperature. The 4s electrons in elemental Cu, Zn and Ni can be easily removed at a relatively low temperature due to their weak attraction to the nucleus, which is the reason why they act as electron donors in the sample. Because both Zn and Ni atoms have two 4s electrons, whereas Cu atom has only one 4s electron, the thermal activation of various $\text{PbM}_{0.01}\text{Se}$ samples leads to the release of a larger fraction of free carriers in the Zn and Ni containing samples compared to the Cu containing sample following the chemical equations (1) through (3).



However, since the 3d orbital of the Cu atom also contains a single electron, further oxidation of the Cu^+ ion obtained from equation (1) is possible, when sufficient energy is provided to break the attractive force tying it to the nuclear charge accordingly to the chemical equation (4).



This explains the sudden increase in the carrier concentration in $\text{PbCu}_{0.01}\text{Se}$ sample upon increasing the temperature beyond 673 K. The complexity of the $\text{PbCu}_{0.01}\text{Se}$ samples is further exacerbated by the potential for the interstitial Cu^+ or Cu^{2+} ions to migrate through the PbSe crystal lattice, as previously observed in other Cu-containing

compounds such as Cu_2Se ³¹ and Cu_7PSe_6 ³². In such mixed ion and electron conducting system, the evaluation and interpretation of thermal and electrical transport properties are quite challenging.

To further understand the complex behavior of Cu, we calculated the formation energies for possible defects in PbSe-Cu system. When the Cu atoms are incorporated into PbSe system, several defects are likely to co-exist including Pb vacancy (V_{Pb}), Cu-filled Pb vacancy (Cu_{Pb}), Cu interstitials (Cu_i), *etc.* The defects formation energies for both Pb-rich and Se-rich conditions as a function of Fermi energy are shown in Fig. S1. It can be seen that the formation energy of Cu_i is lower than that of Cu_{Pb} for Pb-rich condition. On the other hand of Se-rich, the formation energy of Cu_i is higher than Cu_{Pb} when the Fermi level enters the conduction band, which indicates that Cu will first occupy Pb vacancies and then form Cu interstitials. These results are consistent with our previous analysis in PbTe-Cu²³. Additionally, the kinks in the curves refer to the transition energy levels between the different charge states. The curves of Cu_i for both conditions indicate that the formation energy of Cu^+ is lower than that of Cu^{2+} , which support the carrier concentrations of $\text{PbCu}_{0.01}\text{Se}$ at the temperature below 673 K. Unfortunately, we could not get the defects energy at the temperature above 673 K.

The electrical properties of $\text{PbM}_{0.01}\text{Se}$ (M=Cu, Zn, Ni) samples as a function of temperature are shown in Fig. 3. As we expected, the electrical conductivity of PbSe sample is significantly improved with the incorporation of only 1 % of metallic elements. The thermoelectric transport parameters of $\text{PbM}_{0.01}\text{Se}$ (M=Cu, Zn, Ni) at room temperature are shown in Table 1. Regardless of the composition, the electrical conductivity decreases with rising temperature, which is consistent with heavily doped semiconducting behavior. At 300 K, the electrical conductivity of $\text{PbZn}_{0.01}\text{Se}$ and $\text{PbNi}_{0.01}\text{Se}$ samples can reach $\sim 4155 \text{ S cm}^{-1}$ and $\sim 3920 \text{ S cm}^{-1}$, respectively, which are much higher than that of undoped PbSe sample. The electrical conductivity of the $\text{PbCu}_{0.01}\text{Se}$ sample at 300 K is only $\sim 2806 \text{ S cm}^{-1}$, which approximately half that of the former two samples. However, a plateau appears at 673 K on the electrical conductivity of $\text{PbCu}_{0.01}\text{Se}$ samples, whereas the electrical conductivity of the Ni and Zn containing samples continues to decrease. Therefore, the $\text{PbCu}_{0.01}\text{Se}$ sample displays a higher

electrical conductivity than the $\text{PbZn}_{0.01}\text{Se}$ and $\text{PbNi}_{0.01}\text{Se}$ samples at temperatures above 673 K, which is associated to the synergistic effect of the observed large increase in both carrier concentration and mobility in the $\text{PbCu}_{0.01}\text{Se}$ sample.

The temperature dependent Seebeck coefficients of the $\text{PbM}_{0.01}\text{Se}$ (M=Cu, Zn, Ni) samples are displayed in Fig. 3(b). The Seebeck coefficients of $\text{PbZn}_{0.01}\text{Se}$ and $\text{PbNi}_{0.01}\text{Se}$ increase linearly with rising temperature, which is consistent with heavily doped semiconductor behavior.³³ The Seebeck coefficient of $\text{PbCu}_{0.01}\text{Se}$ first increase with increasing temperature, then reached a plateau at 673 K, which is the result of the increase in the carrier concentration.

The calculated powder factor ($S^2\sigma$) of $\text{PbM}_{0.01}\text{Se}$ (M=Cu, Zn, Ni) samples as a function of temperature are shown in Fig. 3(c). It can be seen that the power factor of PbSe has been improved significantly through the introduction of metallic elements with small atom radius. The captivating power factor of $\sim 26.2 \mu\text{W cm}^{-1}\text{K}^{-2}$ and $\sim 24.7 \mu\text{W cm}^{-1}\text{K}^{-2}$ at 523 K can be achieved for the $\text{PbZn}_{0.01}\text{Se}$ and $\text{PbCu}_{0.01}\text{Se}$ samples, respectively, which is a result of the optimized carrier concentration and improved carrier mobility.

To further analyze the measured electrical transport data, the theoretical Pisarenko relationship for n -type PbSe was calculated using a single parabolic band (SPB) model with effective mass $m^*/m_e = 0.36$ (black dotted line).³⁴⁻³⁶ The Seebeck coefficient and carrier concentration can be correlated through the following formulae:³⁷

$$S = \pm \frac{k_B}{e} \left(\frac{(5/2 + r)F_{2/3+r}(\eta)}{(3/2 + r)F_{1/2+r}(\eta)} - \eta \right) \quad (5)$$

$$n = 4\pi \left(\frac{2m^* k_B T}{h^2} \right)^{3/2} F_{1/2}(\eta) \quad (6)$$

where η is the reduced Fermi level, and we choose acoustic phonon scattering as the dominant electron scattering mechanism (the scattering factor $r = -1/2$). The Fermi integral is given by:³⁸

$$F_n(\eta) = \int_0^\infty \frac{x^n}{1 + e^{x-\eta}} dx \quad (7)$$

As depicted in Fig. 3(d), the Seebeck coefficients of $\text{PbM}_{0.01}\text{Se}$ (M=Cu, Zn, Ni) are consistent with the calculated Pisarenko line, which indicated that there is no obvious

change in band structure of PbSe upon introducing the small metallic elements.

The temperature dependent thermal transport properties of the $\text{PbM}_{0.01}\text{Se}$ (M=Cu, Zn, Ni) samples are shown in Fig. 4. The total thermal conductivity is calculated by the formula, $\kappa_{\text{tot}} = D \cdot C_p \cdot \rho$, where D is the thermal diffusivity, C_p is the specific heat capacity estimated with Dulong-Petit Law^{39, 40} and ρ is the sample density determined using the dimensions and mass of the sample, which can be seen in Table 1. As depicted in Fig. 4(c), the total thermal conductivity of the $\text{PbZn}_{0.01}\text{Se}$ and $\text{PbNi}_{0.01}\text{Se}$ samples are similar and higher than that of the $\text{PbCu}_{0.01}\text{Se}$ sample. It is well known that the total thermal conductivity (κ_{tot}) is composed of electronic thermal conductivity (κ_{ele}) and lattice thermal conductivity (κ_{lat}). The electronic thermal conductivity is calculated according to the Wiedemann-Franz law^{41, 42}, $\kappa_{\text{ele}} = L\sigma T$, where the L is the Lorenz number estimated using SPB model and assuming acoustic phonon scattering.^{43, 44} The temperature dependent Lorenz number of the $\text{PbM}_{0.01}\text{Se}$ (M=Cu, Zn, Ni) samples is depicted in Fig. 4(d). Due to the large increase in the carrier mobility and carrier density at 673 K, and the possible diffusion of Cu^+ ions in $\text{PbCu}_{0.01}\text{Se}$ sample, the Lorenz number is nearly constant at temperatures above 673 K, similar to the trend observed on the temperature dependent Seebeck coefficient plot. Consequently, the calculated electronic thermal conductivity at temperatures above 673 K using the Wiedemann-Franz law is nearly constant value for $\text{PbCu}_{0.01}\text{Se}$ sample, shown in Fig. 4(e), which contributes a relatively large value to the total thermal conductivity.

The lattice thermal conductivity calculated by simply subtracting the electronic thermal conductivity from the measured total thermal conductivity is shown in Fig. 4(f).⁴⁵ It can be seen that the lattice thermal conductivity of the $\text{PbCu}_{0.01}\text{Se}$ reaches a negative value at 773 K, which is physically impossible to achieve. Therefore, this implies that strong electron-phonon coupling assumption of the Wiedemann-Franz law is not applicable in the $\text{PbCu}_{0.01}\text{Se}$ sample at temperatures above 673 K, further demonstrating the weak coupling between heat and charge transport in the $\text{PbCu}_{0.01}\text{Se}$ sample at high temperatures. This result implies that the extremely low lattice thermal conductivity reported in many thermoelectric materials could also be resulting from the overestimation of the electronic contribution to the thermal conductivity due to the

application of the Wiedemann-Franz law in systems with weak electron-phonon coupling. Although the κ_{lat} of the $\text{PbCu}_{0.01}\text{Se}$ sample is not calculated correctly at higher temperatures, our result shows that the lattice thermal conductivity of pristine PbSe sample has been decreased significantly through the introduction of metallic elements with small atom radius, especially in low temperature range. For instance, the lattice thermal conductivity decreases from $\sim 2.0 \text{ W m}^{-1}\text{K}^{-1}$ for pristine PbSe to $\sim 0.96 \text{ W m}^{-1}\text{K}^{-1}$ for $\text{PbZn}_{0.01}\text{Se}$ at 300 K, which corresponds to more than 50 % reduction.

To reveal the structural origin of the abnormal electrical and thermal transport behaviors of the $\text{PbCu}_{0.01}\text{Se}$ sample compared to the $\text{PbZn}_{0.01}\text{Se}$ or $\text{PbNi}_{0.01}\text{Se}$ samples, STEM HAADF (high angle annular dark field), which produces contrast interpretable by mass-thickness (the number of atoms) or Z contrast and STEM ABF (annular bright field), which has weaker Z-dependence and is also sensitive to strain^{46, 47}, are performed on $\text{PbCu}_{0.01}\text{Se}$ and $\text{PbZn}_{0.01}\text{Se}$ samples. These two techniques typically used to visualize structural defects at various scales, especially point defects.^{23, 48, 49} As observed in other PbQ (Q=Te, Se, S) systems doped with small-size metallic elements,^{23, 26, 29} both Cu, Zn and Ni fill in the interstitial sites of the PbSe host lattice and form interstitial clusters after compensating the intrinsic Pb vacancies. As shown in Fig. 5(a, b) for $\text{PbCu}_{0.01}\text{Se}$ and Fig. 5(d, e) for $\text{PbZn}_{0.01}\text{Se}$, the density of interstitial clusters, shown as plate-like nanostructures at the low magnification, is much lower (around 1/6) in the $\text{PbCu}_{0.01}\text{Se}$ sample compared to the $\text{PbZn}_{0.01}\text{Se}$ sample. These plate-like nanostructures with certain anisotropy are quite common in PbQ -based thermoelectric systems, while not observed in other thermoelectric materials, even for those who are more sensitive to ion beam, e.g., Sn-based and Cu-based systems. To avoid the possibility of ion beam induced artifacts⁵⁰, the TEM samples were subtly grinded and polished to very thin ($\sim 10 \mu\text{m}$, avoiding long-time ion milling), and then low-voltage (below 3 kV) ion milled and cleaned with very weak voltage (0.1 kV) for a long time, under cooling with liquid N_2 . The structural details of these nanostructures could be revealed clearly as ordered interstitials plates with strain field, whose direction is perpendicular to the interstitial plane, as shown in Fig. 5(b, c1, c2 and e). The interstitial atoms are located at tetrahedral sites with the rocksalt structure of the PbSe the matrix. From the intensity of these

interstitial atoms, it is highly possible that they are also ordered along the observation direction. Furthermore, these ordered interstitial plates induce strong lattice distortions at the interfaces with the PbSe matrix. As expected, strain analysis in Fig. 5(f) based on Fig. 5(e) by geometric phase analysis (GPA) clearly show the strains along interstitial plane direction. The strains induced by the ordered interstitial plates exhibit an anisotropic behavior, and they are mainly distributed along the direction perpendicular to the platelets, which is shown as dark contrast surrounding the interstitial plates. It appears that the nanostructures observed at the low magnification are actually the result from the strain field of the two-layer interstitial plates. When observing along [110] directions, the above nanostructures appear as elliptical, as shown in Fig. 5(g, h). The high-resolution STEM ABF image in Fig. 5 (f, h) clearly shows that there are cores in the middle of such nanostructure. The relative strain analyzed result is shown in Fig. 5(i), where high strain exists at the cores of the nanostructures, i.e., interstitial plates. Such atomic-scale ordered interstitial plates could contribute much to the phonon scattering. The lower density of interstitial plates of PbCu_{0.01}Se means weaker phonon scattering at low temperatures, i.e., higher lattice thermal conductivity, compared with PbZn_{0.01}Se or PbNi_{0.01}Se. However, the introduced Cu atoms possess high potential (as shown in Equ. 4) to further release electrons into the matrix, which is beneficial for electrical transport.

The combination of captivating optimized power factor and the greatly reduced lattice thermal conductivity leads to the extremely improved thermoelectric performance. As shown in Fig. 6(a), a maximum ZT of ~ 1.6 can be achieved for the PbCu_{0.01}Se sample at 773 K and ~ 1.5 can be obtained for the PbZn_{0.01}Se sample at 873 K. The average ZT (ZT_{ave}) is calculated by the following equation:⁵¹

$$ZT_{\text{ave}} = \frac{1}{T_h - T_c} \int_{T_c}^{T_h} ZT \, dT \quad (8)$$

where T_h and T_c are the hot-side and the cold-side temperature, respectively. As depicted in Fig. 6(b), the ZT_{ave} of PbCu_{0.01}Se and PbZn_{0.01}Se can reach ~ 0.96 and ~ 0.84 , respectively, which are improved enormously compared with the ~ 0.44 of pristine PbSe without small metallic elements.

4. Conclusions

In this work, the effects of Cu, Zn and Ni on the thermoelectric properties of *n*-type PbSe were investigated by introducing a small amount of metal elements with small atomic radius. We found that all the three metallic elements act as electron donors in *n*-type PbSe to improve the carrier concentration. The difference is that the Cu⁺ ions will further release electron in the PbCu_{0.01}Se matrix, which leads to an increase of carrier concentration at temperatures higher than 673 K. We also found a weak electron-phonon coupling in the PbCu_{0.01}Se sample at temperatures above 673 K, which is manifested by the observation of a negative value of the lattice thermal negative upon using the Wiedemann-Franz law to estimate the electronic contribution to the total thermal conductivity. This work indicates that the thermoelectric performance of IV-VI compounds can be boosted *via* introducing extra metallic elements with small radius.

Conflicts of interest

The authors declare no competing financial interest.

Acknowledgements

This work was supported by the National Natural Science Foundation of China (51772012 and 51632005), National Key Research and Development Program of China (2018YFA0702100 and 2018YFB0703600), Beijing Natural Science Foundation (JQ18004), Shenzhen Peacock Plan team (KQTD2016022619565991), 111 Project (B17002), the CSC Scholarship and the Academic Excellence Foundation of BUAA for PhD students. H.W. would like to acknowledge the financial support from Singapore Ministry of Education Tier 1 grant, R-284-000-212-114, for Lee Kuan Yew Postdoctoral Fellowship. H.W and S.J.P appreciate the support of the Ministry of Education of Singapore under its Tier 2 (MOE2017-T2-1-129). PFPP thanks the support from the National Science Foundation under Awards DMR-1561008. L.D.Z. thanks for the support from the National Science Foundation for Distinguished Young

Scholars (51925101).

References

- 1 W. K. He, D. Y. Wang, H. J. Wu, Y. Xiao, Y. Zhang, D. S. He, Y. Feng, Y. J. Hao, J. F. Dong, R. Chetty, L. J. Hao, D. F. Chen, J. F. Qin, Q. Yang, X. Li, J. M. Song, Y. C. Zhu, W. Xu, C. L. Niu, X. Li, G. T. Wang, C. Liu, M. Ohta, S. J. Pennycook, J. Q. He, J. F. Li and L. D. Zhao, *Science*, 2019, **365**, 1418-1424.
- 2 Y. M. Zhou and L. D. Zhao, *Adv. Mater.*, 2017, **29**, 1702676.
- 3 Y. Xiao, H. J. Wu, J. Cui, D. Y. Wang, L. W. Fu, Y. Zhang, Y. Chen, J. Q. He, S. J. Pennycook and L. D. Zhao, *Energy Environ. Sci.*, 2018, **11**, 2486-2495.
- 4 Y. Wu, Q. Lou, Y. Qiu, J. Guo, Z. Y. Mei, X. Xu, J. Feng, J. Q. He and Z. H. Ge, *Inorg. Chem. Front.*, 2019, **6**, 1374-1381.
- 5 X. Wang, X. Li, Z. Zhang, X. Li, C. Chen, S. Li, X. Lin, J. Sui, X. Liu, F. Cao, J. Yang and Q. Zhang, *Mater. Today Phys.*, 2018, **6**, 45-52.
- 6 P. J. Ying, X. H. Liu, C. G. Fu, X. Q. Yue, H. H. Xie, X. B. Zhao, W. Q. Zhang and T. J. Zhu, *Chem. Mater.*, 2015, **27**, 909-913.
- 7 Q. H. Zhang, J. C. Liao, Y. S. Tang, M. Gu, C. Ming, P. F. Qiu, S. Q. Bai, X. Shi, C. Uher and L. D. Chen, *Energy Environ. Sci.*, 2017, **10**, 956-963.
- 8 C. Chang, M. H. Wu, D. S. He, Y. L. Pei, C. F. Wu, X. F. Wu, H. L. Yu, F. Y. Zhu, K. D. Wang, Y. Chen, L. Huang, J. F. Li, J. Q. He and L. D. Zhao, *Science*, 2018, **360**, 778-782.
- 9 G. J. Tan, X. M. Zhang, S. Q. Hao, H. Chi, T. P. Bailey, X. L. Su, C. Uher, V. P. Dravid, C. Wolverton and M. G. Kanatzidis, *ACS Appl. Mater. Interfaces*, 2019, **11**, 9197-9204.
- 10 G. J. Tan, L. D. Zhao and M. G. Kanatzidis, *Chem. Rev.*, 2016, **116**, 12123-12149.
- 11 Y. Xiao, H. J. Wu, D. Y. Wang, C. L. Niu, Y. L. Pei, Y. Zhang, I. Spanopoulos, I. T. Witting, X. Li, S. J. Pennycook, G. J. Snyder, M. G. Kanatzidis and L. D. Zhao, *Adv. Energy Mater.*, 2019, **9**, 1900414.
- 12 X. Qian, Y. Xiao, C. Chang, L. Zheng and L. D. Zhao, *Prog. Nat. Sci-Mater.*, 2018, **28**, 275-280.
- 13 Y. Z. Pei, X. Y. Shi, A. LaLonde, H. Wang, L. D. Chen and G. J. Snyder, *Nature*, 2011, **473**, 66-69.
- 14 Z. W. Chen, Z. Z. Jian, W. Li, Y. J. Chang, B. H. Ge, R. Hanus, J. Yang, Y. Chen, M. X. Huang, G. J. Snyder and Y. Z. Pei, *Adv. Mater.*, 2017, **29**, 1606768.
- 15 J. P. Heremans, B. Wiendlocha and A. M. Chamoire, *Energy Environ. Sci.*, 2012, **5**, 5510-5530.
- 16 Q. Y. Zhang, H. Wang, W. S. Liu, H. Z. Wang, B. Yu, Q. Zhang, Z. T. Tian, G. Ni, S. Lee, K. Esfarjani, G. Chen and Z. F. Ren, *Energy Environ. Sci.*, 2012, **5**, 5246-5251.
- 17 K. Biswas, J. Q. He, I. D. Blum, C. I. Wu, T. P. Hogan, D. N. Seidman, V. P. Dravid and M. G. Kanatzidis, *Nature*, 2012, **489**, 414-418.
- 18 G. J. Tan, S. Q. Hao, S. T. Cai, T. P. Bailey, Z. Z. Luo, I. Hadar, C. Uher, V. P. Dravid, C. Wolverton and M. G. Kanatzidis, *J. Am. Chem. Soc.*, 2019, **141**, 4480-4486.
- 19 T. J. Zhu, Y. T. Liu, C. G. Fu, J. P. Heremans, J. G. Snyder and X. B. Zhao, *Adv. Mater.*, 2017, **29**, 1605884.
- 20 H. Wang, Z. M. Gibbs, Y. Takagiwa and G. J. Snyder, *Energy Environ. Sci.*, 2014, **7**, 804-811.
- 21 X. Qian, L. Zheng, Y. Xiao, C. Chang and L. D. Zhao, *Inorg. Chem. Front.*, 2017, **4**, 719-726.
- 22 D. Wu, L. D. Zhao, X. Tong, W. Li, L. J. Wu, Q. Tan, Y. L. Pei, L. Huang, J. F. Li, Y. M. Zhu, M.

- G. Kanatzidis and J. Q. He, *Energy Environ. Sci.*, 2015, **8**, 2056-2068.
- 23 Y. Xiao, H. J. Wu, W. Li, M. J. Yin, Y. L. Pei, Y. Zhang, L. W. Fu, Y. X. Chen, S. J. Pennycook, L. Huang, J. He and L. D. Zhao, *J. Am. Chem. Soc.*, 2017, **139**, 18732-18738.
- 24 Y. R. Gong, C. Chang, W. Wei, J. Liu, W. J. Xiong, S. Chai, D. Li, J. Zhang and G. D. Tang, *Scr. Mater.*, 2018, **147**, 74-78.
- 25 Y. Z. Pei, A. F. May and G. J. Snyder, *Adv. Energy Mater.*, 2011, **1**, 291-296.
- 26 X. Qian, H. Wu, D. Wang, Y. Zhang, S. J. Pennycook, X. Gao, L. Zheng and L. D. Zhao, *Mater. Today Phys.*, 2019, **9**, 100102.
- 27 L. You, Y. F. Liu, X. Li, P. F. Nan, B. H. Ge, Y. Jiang, P. F. Luo, S. S. Pan, Y. Z. Pei, W. Q. Zhang, G. J. Snyder, J. Yang, J. Y. Zhang and J. Luo, *Energy Environ. Sci.*, 2018, **11**, 1848-1858.
- 28 Q. Zhang, E. K. Chere, K. McEnaney, M. L. Yao, F. Cao, Y. Z. Ni, S. Chen, C. Opeil, G. Chen and Z. F. Ren, *Adv. Energy Mater.*, 2015, **5**, 1401977.
- 29 M. H. Zhao, C. Chang, Y. Xiao, R. Gu, J. Q. He and L. D. Zhao, *J. Alloys Compd.*, 2019, **781**, 820-830.
- 30 D. L. Dexter and F. Seitz, *Phys. Rev.*, 1952, **86**, 964-965.
- 31 A. A. Olvera, N. A. Moroz, P. Sahoo, P. Ren, T. P. Bailey, A. A. Page, C. Uher and P. F. P. Poudeu, *Energy Environ. Sci.*, 2017, **10**, 1668-1676.
- 32 F. Baumer and T. Nilges, *Z. Anorg. Allg. Chem.*, 2018, **644**, 1519-1524.
- 33 J. Androulakis, D. Y. Chung, X. L. Su, L. Zhang, C. Uher, T. C. Hasapis, E. Hatzikraniotis, K. M. Paraskevopoulos and M. G. Kanatzidis, *Phys. Rev. B*, 2011, **84**, 155207.
- 34 J. P. Heremans, V. Jovovic, E. S. Toberer, A. Saramat, K. Kurosaki, A. Charoenphakdee, S. Yamanaka and G. J. Snyder, *Science*, 2008, **321**, 554-557.
- 35 Q. Zhang, F. Cao, K. Lukas, W. S. Liu, K. Esfarjani, C. Opeil, D. Broido, D. Parker, D. J. Singh, G. Chen and Z. F. Ren, *J. Am. Chem. Soc.*, 2012, **134**, 17731-17738.
- 36 A. F. May, E. S. Toberer, A. Saramat and G. J. Snyder, *Phys. Rev. B*, 2009, **80**, 125205.
- 37 H. J. Wu, C. Chang, D. Feng, Y. Xiao, X. Zhang, Y. L. Pei, L. Zheng, D. Wu, S. K. Gong, Y. Chen, J. Q. He, M. G. Kanatzidis and L. D. Zhao, *Energy Environ. Sci.*, 2015, **8**, 3298-3312.
- 38 C. F. Wu, H. Wang, Q. M. Yan, T. R. Wei and J. F. Li, *J. Mater. Chem. C*, 2017, **5**, 10881-10887.
- 39 K. Biswas, J. Q. He, Q. C. Zhang, G. Y. Wang, C. Uher, V. P. Dravid and M. G. Kanatzidis, *Nat. Chem.*, 2011, **3**, 160-166.
- 40 Y. Xiao, W. Li, C. Chang, Y. X. Chen, L. Huang, J. Q. He and L. D. Zhao, *J. Alloys Compd.*, 2017, **724**, 208-221.
- 41 L. D. Zhao, V. P. Dravid and M. G. Kanatzidis, *Energy Environ. Sci.*, 2014, **7**, 251-268.
- 42 Y. L. Pei, C. Chang, Z. Wang, M. J. Yin, M. H. Wu, G. J. Tan, H. J. Wu, Y. X. Chen, L. Zheng, S. K. Gong, T. J. Zhu, X. B. Zhao, L. Huang, J. Q. He, M. G. Kanatzidis and L. D. Zhao, *J. Am. Chem. Soc.*, 2016, **138**, 16364-16371.
- 43 H. Mori, H. Usui, M. Ochi and K. Kuroki, *Phys. Rev. B*, 2017, **96**, 085113.
- 44 Y. Z. Pei, A. D. LaLonde, N. A. Heinz, X. Y. Shi, S. Iwanaga, H. Wang, L. D. Chen and G. J. Snyder, *Adv. Mater.*, 2011, **23**, 5674-5678.
- 45 G. J. Snyder and E. S. Toberer, *Nat. Mater.*, 2008, **7**, 105-114.
- 46 H. J. Wu, X. X. Zhao, D. S. Song, F. Tian, J. Wang, K. P. Loh and S. J. Pennycook, *Ultramicroscopy*, 2018, **194**, 182-192.
- 47 H. J. Wu, X. X. Zhao, C. Guan, L. D. Zhao, J. G. Wu, D. S. Song, C. J. Li, J. Wang, K. P. Loh, T. V. Venkatesan and S. J. Pennycook, *Adv. Mater.*, 2018, **30**, 1802402.

- 48 H. J. Wu, Y. Zhang, S. C. Ning, L. D. Zhao and S. J. Pennycook, *Mater. Horiz.*, 2019, **6**, 1548-1570.
- 49 B. C. Qin, D. Y. Wang, W. K. He, Y. Zhang, H. J. Wu, S. J. Pennycook and L. D. Zhao, *J. Am. Chem. Soc.*, 2019, **141**, 1141-1149.
- 50 X. M. Zhang, S. Q. Hao, G. J. Tan, X. B. Hu, E. W. Roth, M. G. Kanatzidis, C. Wolverton and V. P. Dravid, *Microsc. Microanal.*, 2019, **25**, 831-839.
- 51 X. Zhang and L.-D. Zhao, *J. Materiomics*, 2015, **1**, 92-105.

Table 1. Thermoelectric transport parameters of $\text{PbM}_{0.01}\text{Se}$ (M=Cu, Zn, Ni) at room temperature.

sample	n_{H} (10^{19} cm^{-3})	μ_{H} ($\text{cm}^2 \text{ V}^{-1} \text{ s}^{-1}$)	σ (S cm^{-1})	S ($\mu\text{V K}^{-1}$)	κ_{lat} ($\text{W m}^{-1}\text{K}^{-1}$)	ρ (g cm^{-3})	ZT_{max}
PbSe	0.97	18	29	-174	2.00	8.003	0.76
PbCu _{0.01} Se	2.30	716	2807	-73	1.32	7.903	1.63
PbZn _{0.01} Se	3.50	693	4155	-64	0.96	7.983	1.50
PbNi _{0.01} Se	3.43	756	3920	-66	1.03	7.952	1.37

n_{H} , carrier concentration; μ_{H} , carrier mobility; σ , electrical conductivity; S , Seebeck coefficient; κ_{lat} , lattice thermal conductivity; ρ , measured sample density; ZT_{max} , maximum ZT value.

Figure captions

Figure 1. Powder XRD patterns of $\text{PbM}_{0.01}\text{Se}$ (M=Cu, Zn, Ni) samples.

Figure 2. (a) Carrier concentration and (b) carrier mobility for $\text{PbM}_{0.01}\text{Se}$ (M=Cu, Zn, Ni) samples as a function of temperature.

Figure 3. Temperature dependence of the electrical transport properties for $\text{PbM}_{0.01}\text{Se}$ (M=Cu, Zn, Ni) samples: (a) electrical conductivity, (b) Seebeck coefficient, (c) power factor, and (d) the black dotted line is the theoretical Pisarenko relationship for *n*-type PbSe, which is calculated using SPB model with effective mass $m^* = 0.36 m_e$. The reported data of $\text{Pb}_{1-x}\text{B}_x\text{Se}^{35}$, $\text{Pb}_{1-x}\text{Ga}_x\text{Se}^{35}$ and $\text{Pb}_{1-x}\text{In}_x\text{Se}^{35}$ are also plotted for comparison.

Figure 4. Temperature dependence of the thermal transport properties for the $\text{PbM}_{0.01}\text{Se}$ (M=Cu, Zn, Ni) samples: (a) thermal diffusivity, (b) specific heat capacity, (c) total thermal conductivity, (d) Lorenz number, (e) electronic thermal conductivity, and (f) lattice thermal conductivity.

Figure 5. Microstructure of $\text{PbCu}_{0.01}\text{Se}$ and $\text{PbZn}_{0.01}\text{Se}$. (a) Low-magnification STEM ABF image of $\text{PbCu}_{0.01}\text{Se}$ showing a low density of nanostructures along [001] zone axis. (b) High-magnification STEM ABF image of $\text{PbCu}_{0.01}\text{Se}$ image showing one nanostructure. (c1, c2) Simultaneously-acquired atomically-resolved STEM HAADF and ABF images focusing one ordered interstitial plate. (d) Low-magnification STEM ABF image of $\text{PbZn}_{0.01}\text{Se}$ showing a high density of nanostructures along [001] zone axis. (e) High-magnification STEM ABF image of $\text{PbZn}_{0.01}\text{Se}$ image showing six nanostructures. (f) GPA strain analyzed results of (e). (g) Low-magnification STEM ABF image of $\text{PbZn}_{0.01}\text{Se}$ showing a high density of nanostructures [110] zone axis. (h) High-magnification STEM ABF image of $\text{PbZn}_{0.01}\text{Se}$ image showing several nanostructures. (i) GPA strain analyzed result of (h).

Figure 6. (a) *ZT* values for $\text{PbM}_{0.01}\text{Se}$ (M=Cu, Zn, Ni) samples as a function of temperature and (b) average *ZT* comparisons.

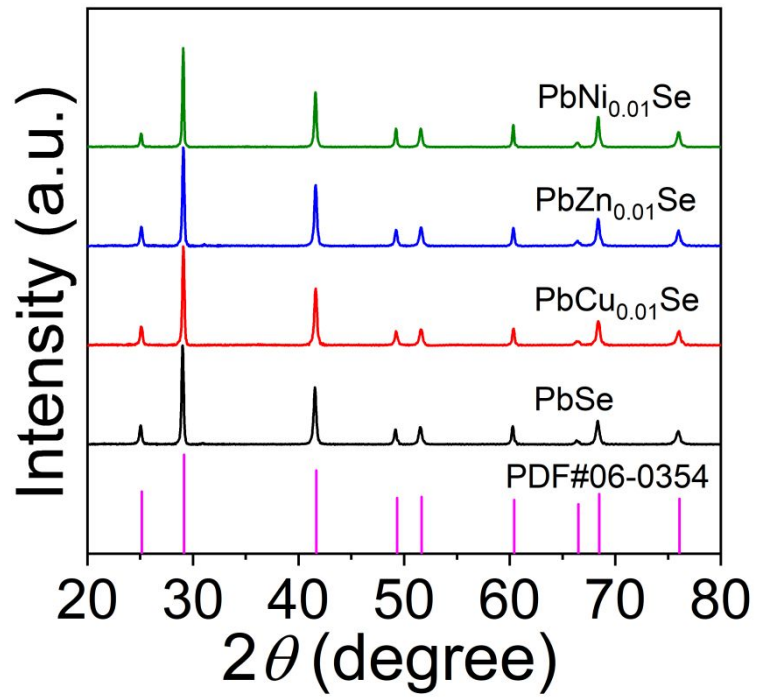


Figure 1

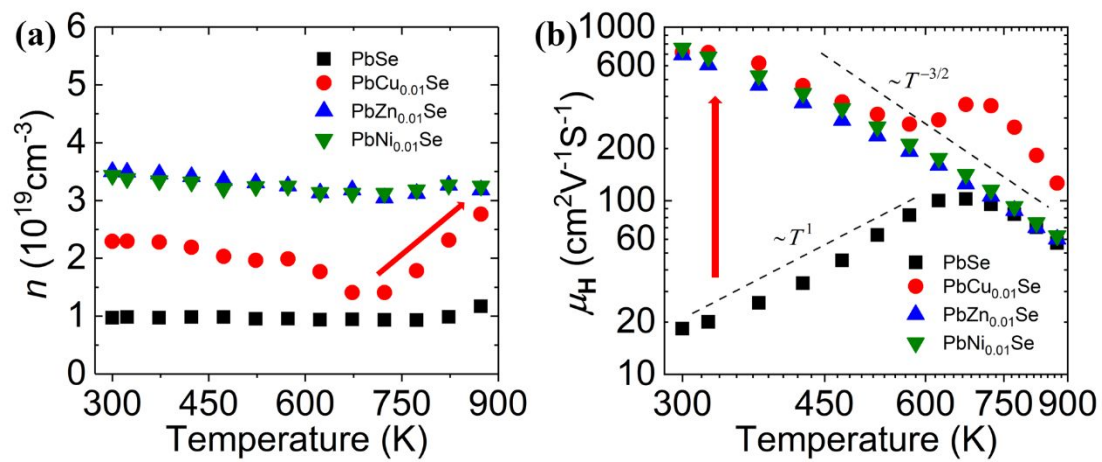


Figure 2

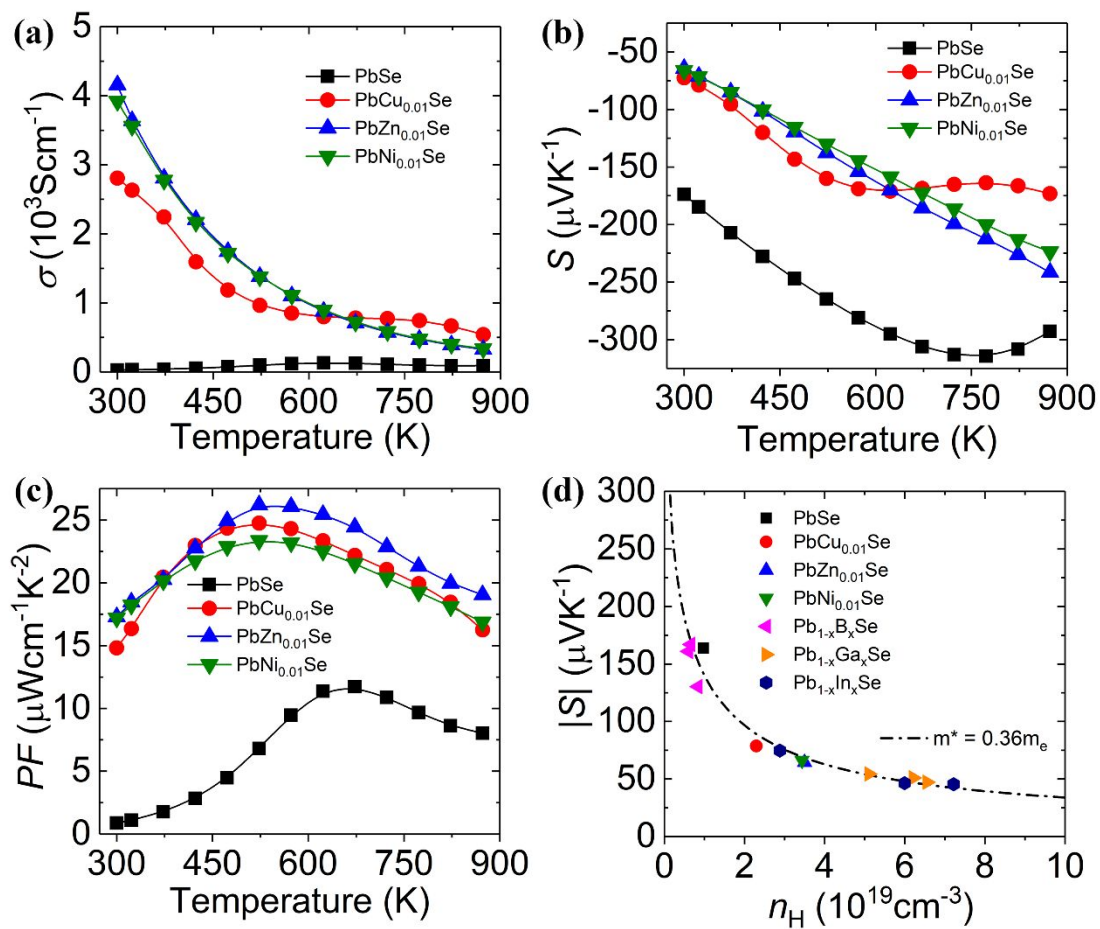


Figure 3

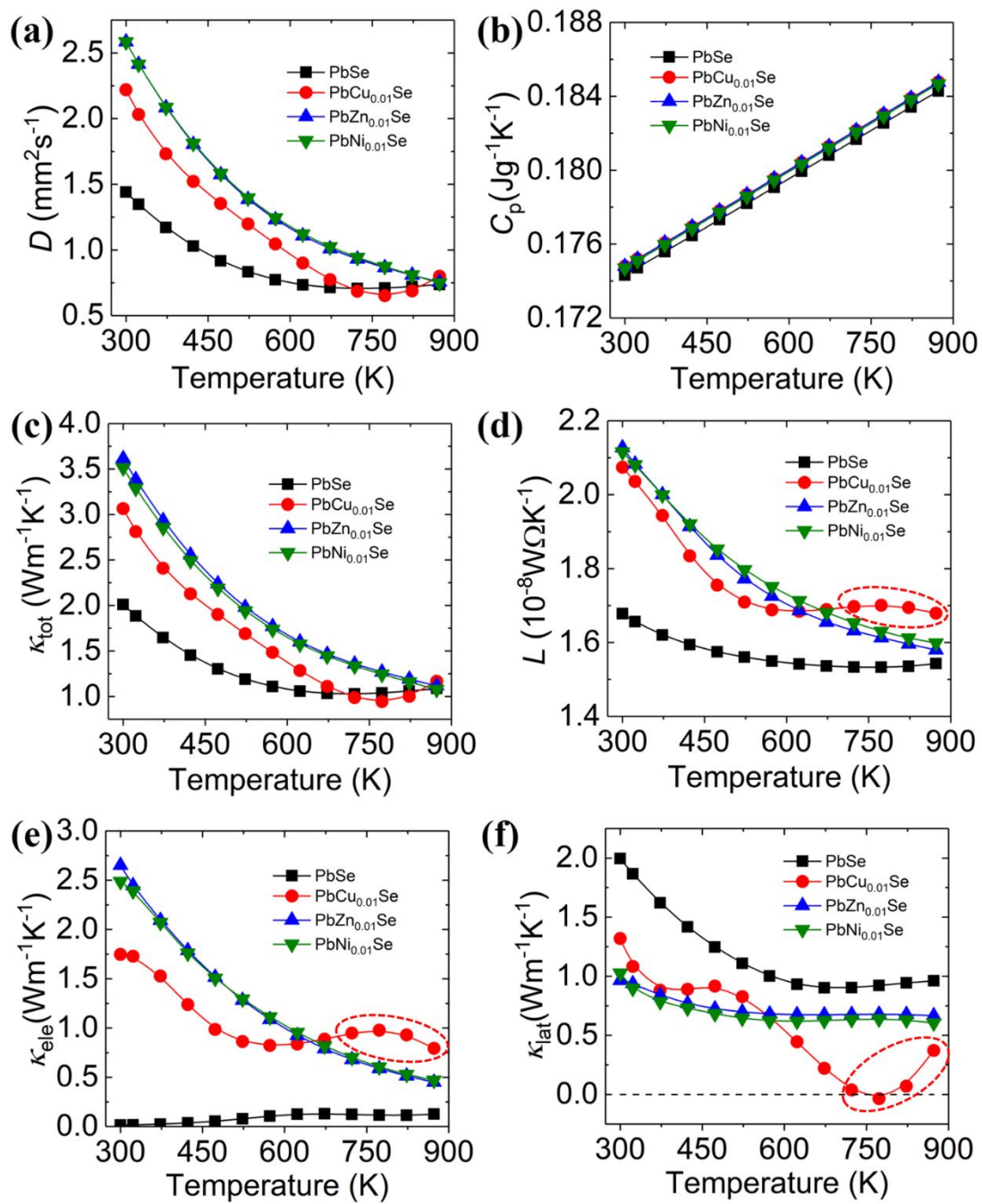
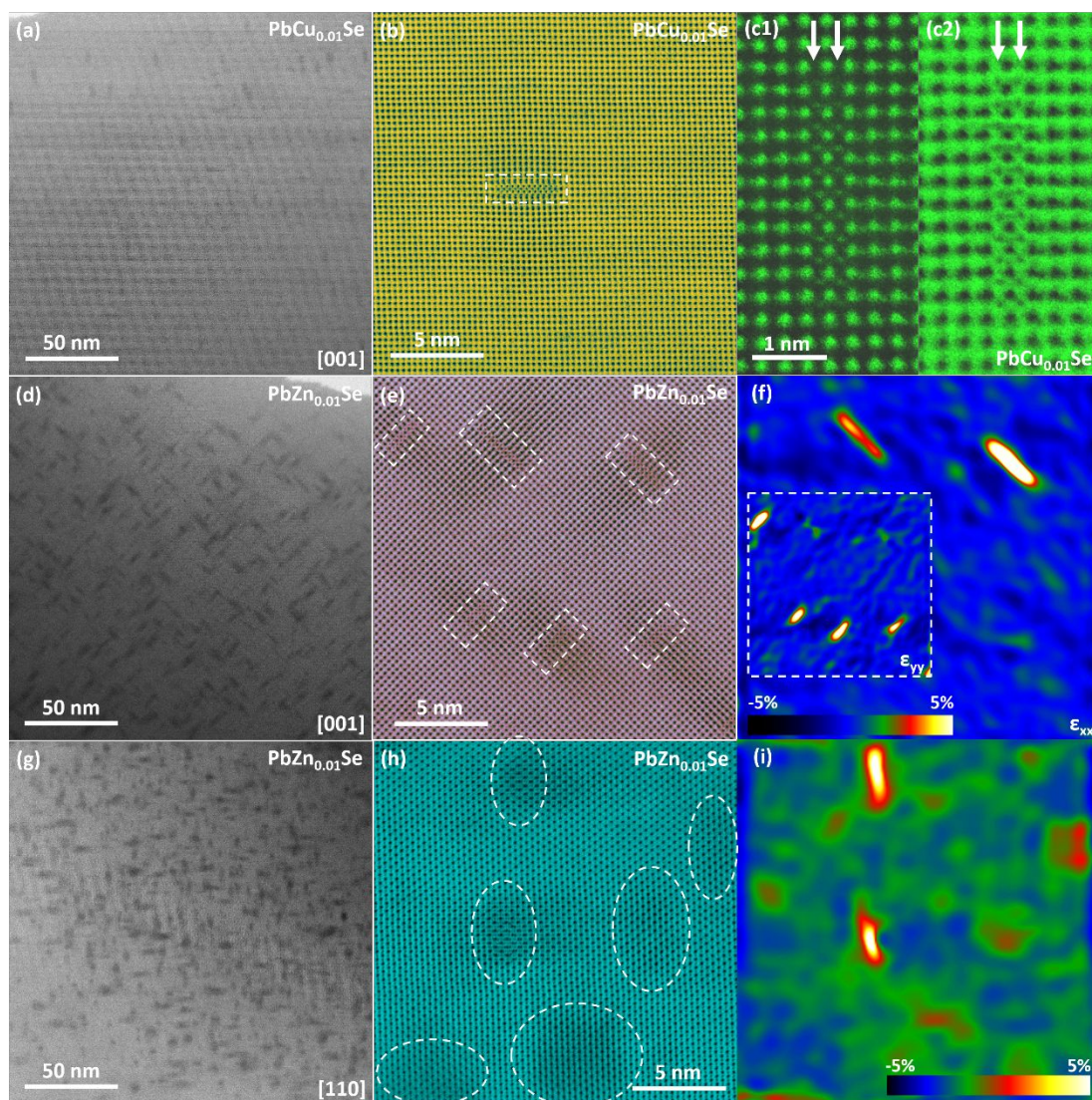


Figure 4

**Figure 5**

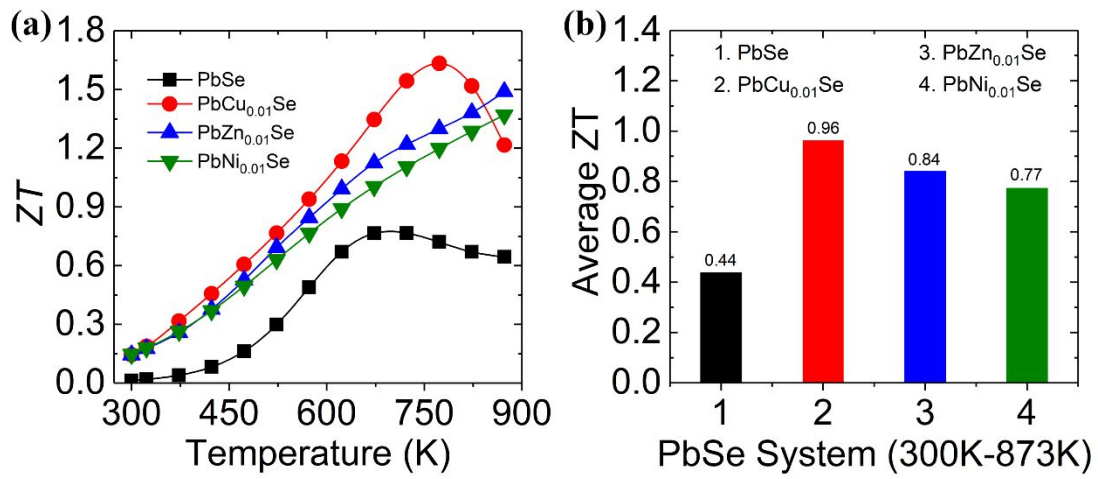
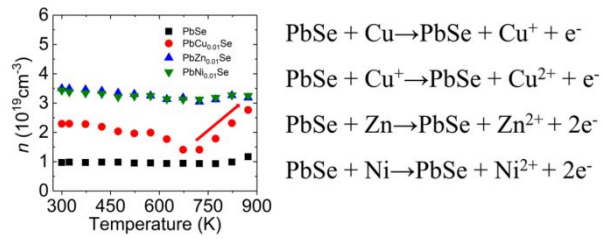


Figure 6

TOC



The carrier concentration of $\text{PbCu}_{0.01}\text{Se}$ sample increases suddenly, which results from the release of 3d orbital electrons in Cu^+ ions.